Trapped photons: Transverse plasmons in layered semiconducting heterostructures

Golenić, Neven; Despoja, Vito

Letter

Trapped photons: Transverse plasmons in layered semiconducting heterostructures

Neven Golenić [1,2] and Vito Despoja [3,4,*]

[1]*Scuola Internazionale Superiore di Studi Avanzati (SISSA), Via Bonomea 265, 34136 Trieste, Italy*
[2]*Department of Physics, University of Zagreb, Bijenička 32, 10000 Zagreb, Croatia*
[3]*Centre for Advanced Laser Techniques, Institute of Physics, Bijenička 46, 10000 Zagreb, Croatia*
[4]*Donostia International Physics Center (DIPC), P. Manuel de Lardizabal, 4, 20018 San Sebastián, Spain*

We elucidate the properties of a robust transverse polarization mode in heterostructures of transition metal dichalcogenides. This *trapped-photon* mode arises from strong interband light-matter coupling, but its nature is fundamentally distinct from extensively studied exciton polaritons, as well as photon-cavity modes. It can be viewed as a transverse counterpart to the longitudinal two-dimensional Dirac plasmon mode found in doped graphene, characterized by much greater oscillatory strength. Furthermore, the trapped photon is easily tunable by adjusting the number of semiconducting layers, allowing for enhanced photon-electron-hole binding strength. In addition, we devise a near-field microscopy simulation that paves the way for future experimental characterization, which could lead to exciting applications in optoelectronics, sensing, and quantum information processing.

Similar to doped graphene, which supports a longitudinal polarization mode known as the Dirac plasmon polariton (DPP) [1], we demonstrate that any semiconducting two-dimensional (2D) crystals, such as transition metal dichalcogenides (TMDs) and hexagonal boron nitride (hBN) in either single-layer or van der Waals heterostructures, can support a transverse polarization mode. This mode generates a current perpendicular to its propagation direction and its electric field is evanescent, causing it to behave akin to a *trapped photon* (T-ph) within the 2D crystal.

T-ph forms from interband electron-hole transitions, and not necessarily from excitons; it can be classified as a semiconducting transverse plasmon polariton, and accordingly it is a counterpart to the longitudinal DPP observed in doped graphene. Moreover, we prove that T-ph exists in any 2D configuration that supports dipole-active interband electronic transitions, which can be easily generalized to IR-active phonons [2–7]. The transverse polarization eigenmode was theoretically predicted even in simple 3D electron gas supported only by an intraband continuum [8]. This suggests that T-ph could exist even in noble metals (Ag and Au) supporting strong $s - d$ interband transitions. A similar phenomenon, the transversal plasmon (T-pl) in doped single-layer graphene (Gr), was theoretically predicted by Mikhailov *et al.* [9]. Another *ab initio* calculation for Gr reveals that its transversal dielectric function Re[$\epsilon_x(Q_y, \omega)$] exhibits a *kink* [10] but never crosses zero [2], hence the formation of transverse plasmons *does not* occur in single-layer graphene.

In Ref. [11] the authors concluded that T-pl is more pronounced in bilayer Gr rather than in a single layer. Yet, our *ab*

initio results for a Gr/hBN bilayer show that its transversal dielectric function Re[$\epsilon_x(Q_y, \omega)$] barely crosses zero only in the ideal case (zero damping limit, $\eta \to 0$, and in heavily doped graphene), right next to the radiative continuum ($\omega > Q_y c$) [2]. On the other hand, in the Gr/hBN trilayer, Re[$\epsilon_x(Q_y, \omega)$] more convincingly crosses zero and T-pl is finitely separated from the radiative continuum ($\omega > Q_y c$), classifying it as a well-defined bosonic eigenmode [2].

It should be emphasized that the T-ph reported in the present Letter does not correspond to the widely investigated exciton polariton observed in TMDs placed in different cavity setups [12–29]. Some recent *cavity-free* experimental studies, where nanostructures such as WS_2 disks [30], nanotubes [31], WS_2 grating [32,33], or WS_2 multilayers [34], are used to achieve Fabry-Pérot resonant (or cavity) modes are still mostly focused on exploring the exciton-cavity-photon hybridization.

In this Letter, we systematically and comparatively explore the oscillatory strengths of T-ph, T-pl, and DPP in alternating WS_2/hBN and Gr/hBN multilayered heterostructures as a function of the number N of WS_2 or Gr layers. Additionally, we quantify the quasibosonic character of T-ph by defining a bending [or longitudinal-transverse (L-T) splitting] parameter $\Omega = \omega_L - \omega_T$. Our calculations reveal that the oscillatory strength of the T-ph mode in the WS_2/hBN bilayer is 29 times greater than that of the T-pl mode, and even seven times greater than that of the DPP mode in a heavily doped Gr/hBN bilayer. Moreover, the obtained T-ph bending Ω for WS_2 is 25 times larger than in the Gr bilayer. In spite of the lack of experimental evidence for T-ph due to its evanescent character, we demonstrate that T-ph is no more difficult to measure than the widely observed DPP [35–37] by simulating the currents induced in a scattering-type scanning near-field optical microscopy (s-SNOM) experiment.

*vdespoja@ifs.hr

The model system investigated here is a WS_2/hBN heterostructure obtained by alternate stacking of hBN and WS_2 single layers parallel to the x-y plane, as illustrated in Fig. S1 of the Supplemental Material (SM) [2]. An important point to note is that hBN, being a wide band gap semiconductor, effectively prevents any spatial and energetic overlap between WS_2 layers. For comparison, we also investigated electromagnetic modes in alternating Gr/hBN heterostructures, which, similar to WS_2/hBN heterostructures, are both widely studied and experimentally feasible [37–42].

The electromagnetic modes in WS_2/hBN heterostructures are analyzed in terms of the screened conductivity tensor

$$\sigma_{\mu\nu}(\mathbf{Q}, \omega) = l\sigma_{\mu\nu g=0, g'=0}(\mathbf{Q}, \omega), \quad (1)$$

where $\mathbf{Q} = (Q_y, Q_y)$ is the transfer wave vector in the x-y plane and $g = 2\pi n/l$ is the reciprocal wave vector in the z direction, where $n \in \mathbb{Z}$ and l is the superlattice constant in the z direction [2]. We neglected the crystal local field effects in the x-y direction while keeping the spatial dispersivity in the z direction, thus if $\mathbf{G} = (\mathbf{G}_\parallel, g)$ is a wave vector in the reciprocal space we have $\mathbf{G}_\parallel = (G_x, G_y) = (0, 0)$, allowing for partial Fourier transforms in the z direction. We then define the screened conductivity hypertensor as

$$\sigma_{\mu\nu gg'}(\mathbf{Q}, \omega) = \sum_{g_1\alpha} \epsilon^{-1}_{\mu\alpha gg_1}(\mathbf{Q}, \omega)\hat{\sigma}^0_{\alpha\nu g_1 g'}(\mathbf{Q}, \omega), \quad (2)$$

where $\hat{\sigma}^0 = \hat{\sigma}^{\mathrm{RPA}} + \hat{\sigma}^{\mathrm{ladd}}$ is the unscreened conductivity or photon self-energy. It comprises two contributions, the first ($\hat{\sigma}^{\mathrm{RPA}}$) being the random phase approximation (RPA) conductivity, which considers only the electron-hole bubble diagram, while the latter ($\hat{\sigma}^{\mathrm{ladd}}$) represents the ladder conductivity, which takes into account electron-hole interactions, and thus includes excitonic effects [6]. The dielectric hypertensor is defined as

$$\epsilon_{\mu\alpha gg'}(\mathbf{Q}, \omega) = \mathbb{I}_{\mu\alpha gg'} - \sum_{g_1\beta} \hat{\sigma}^0_{\mu\beta gg_1}(\mathbf{Q}, \omega)\Gamma_{\beta\alpha g_1 g'}(\mathbf{Q}, \omega), \quad (3)$$

where $\mathbb{I}_{\mu\alpha gg'}$ is a unit matrix, and the free-photon propagator hypertensor [2] is

$$\hat{\Gamma}_{\mu\nu gg'}(\mathbf{Q}, \omega) = \frac{1}{l}\int_{-l/2}^{l/2} e^{-igz}\hat{\Gamma}_{\mu\nu}(\mathbf{Q}, \omega, z, z')e^{ig'_z z'}dzdz', \quad (4)$$

where the free-photon propagator in real (z) space is

$$\hat{\Gamma}(\mathbf{Q}, \omega, z, z') = -\frac{4\pi i}{\omega}\delta(z - z')\mathbf{z} \cdot \mathbf{z}$$
$$- \frac{2\pi}{\omega\beta}\{\hat{E}^s + \hat{E}^p(z, z')\}e^{i\beta|z-z'|}, \quad (5)$$

where E_s and E_p are directional quantities related to s and p polarization [2]. More details on the *ab initio* calculation of $\hat{\sigma}^{\mathrm{RPA}}$ and $\hat{\sigma}^{\mathrm{ladd}}$, as well as the free-photon propagator $\hat{\Gamma}$, which excludes the spurious intersupercell interaction, can be found in SM Sec. S2 [2].

Now, suppose that the system is driven by an external electrical field $\mathbf{E}_0$, then the induced current is $\mathbf{j}^{\mathrm{ind}} = \hat{\sigma}_0\mathbf{E}$, where $\mathbf{E} = \mathbf{E}_0 + \mathbf{E}^{\mathrm{ind}}$ is the total field. Because the induced field is $\mathbf{E}^{\mathrm{ind}} = \hat{\Gamma}\mathbf{j}^{\mathrm{ind}} = \hat{\Gamma}\hat{\sigma}_0\mathbf{E}$, the total field satisfies the following equation,

$$\mathbf{E} = \mathbf{E}_0 + \hat{\Gamma}\hat{\sigma}_0\mathbf{E}.$$

Therefore, the screened electrical field $\mathbf{E}$ and driving field $\mathbf{E}_0$ are connected by the dielectric hypertensor as

$$\hat{\epsilon}(\mathbf{Q}, \omega)\mathbf{E} = \mathbf{E}_0. \quad (6)$$

In the absence of an external field $\mathbf{E}_0 = 0$, Eq. (6) reduces to an eigenvalue problem, where the zero points

$$\mathrm{Re}\{\det\hat{\epsilon}(\mathbf{Q}, \omega)\} = 0$$

determine the dispersion relations of electromagnetic eigenmodes $\omega_T(\mathbf{Q})$,[1] whose oscillatory strength is defined as [2]

$$f^{-1}_\mu(\mathbf{Q}) = \frac{1}{\omega_T}\frac{\partial}{\partial\omega}\mathrm{Im}\left[\frac{1}{\sigma_\mu(\mathbf{Q}, \omega_T)}\right]. \quad (7)$$

The external radiation excites only radiative electromagnetic modes, for example, along the optical absorption pathway in Fig. 1(b). Absorption measurements of WS_2 single layer [14] [blue dots in Fig. 1(c)(i)] reveal three peaks: the A and B excitons, as well as a strong interband resonance C. The normalized screened conductivity $\mathrm{Re}[\sigma_{xx}]/N$ calculated along the optical absorption pathway (black line) for WS_2/hBN trilayer ($N = 3$) shows good agreement with experiment. All subsequent results in the text stem from our theoretical calculations, with the only comparison with the experiment shown in Fig. 1(c)(i). By contrast, evanescent electromagnetic modes can be excited, for example, along the theoretical pathway shown in Fig. 1(b). In Fig. 1(c)(ii), along the theoretical pathway for $Q_y = \omega_A/c = 0.01$ nm^{-1} in the WS_2/hBN trilayer, $\mathrm{Re}[\sigma_{xx}]/N$ shows strong suppression of the A exciton and a sharp peak emerging just below the radiative continuum at $\omega_T < \omega_A$. Because $\mathrm{Re}[\det\hat{\epsilon}]$ (depicted by the green dashed line) then crosses zero, this peak represents a well-defined eigenmode (or boson) that we identified as the *trapped-photon* (T-ph) mode. T-ph due to its evanescent character ($\omega_T < Q_A c$) could be measured in the s-SNOM experiment as illustrated in Fig. 1(a). There the incident monochromatic radiation ω_T excites dipole-active plasmons in the subwavelength SNOM tip and scatters into radiative (far-field) $Q < \omega_T/c$ and evanescent (near-field) $Q > \omega_T/c$ partial waves, along the SNOM pathway depicted in Fig. 1(b). By imaging the scattered (reflected) field, we gain information about the electromagnetic modes in the surrounding van der Waals heterostructure. Figure 1(c)(iii) depicts $\mathrm{Re}[\sigma_{xx}/N]$ in the WS_2/hBN trilayer calculated along the SNOM pathway $\mathbf{Q} = (0, Q_y)$, where the driving frequency $\omega_T = 1.96$ eV. In this case, the presence of a sharp peak and the concomitant vanishing of the dielectric matrix at $Q_y = Q_A$ conclusively confirm the existence/emergence of T-ph.

Figures 1(d)(i)–1(d)(iii) illustrate the (Q_y, ω) scan of $\mathrm{Re}[\sigma_{xx}]/N$ in WS_2 single layer ($N = 1$), WS_2/hBN trilayer ($N = 3$), and five layers ($N = 5$), respectively. The intensive patterns emphasize T-ph dispersion relations $\omega_T(Q_y)$. Already for $N = 1$, T-ph appears as an intensive eigenmode, and for $N = 3$ and 5 it increasingly separates (bends) from the radiative continuum edge Qc. Evidently, T-ph is a quasiboson than can be characterized by two parameters: the oscillator

---

[1] In the derivation of the L and T modes we used reduced units ($\hbar = 1$, $m = 1$, $c = 1$, and $e = 1$) for simplicity.
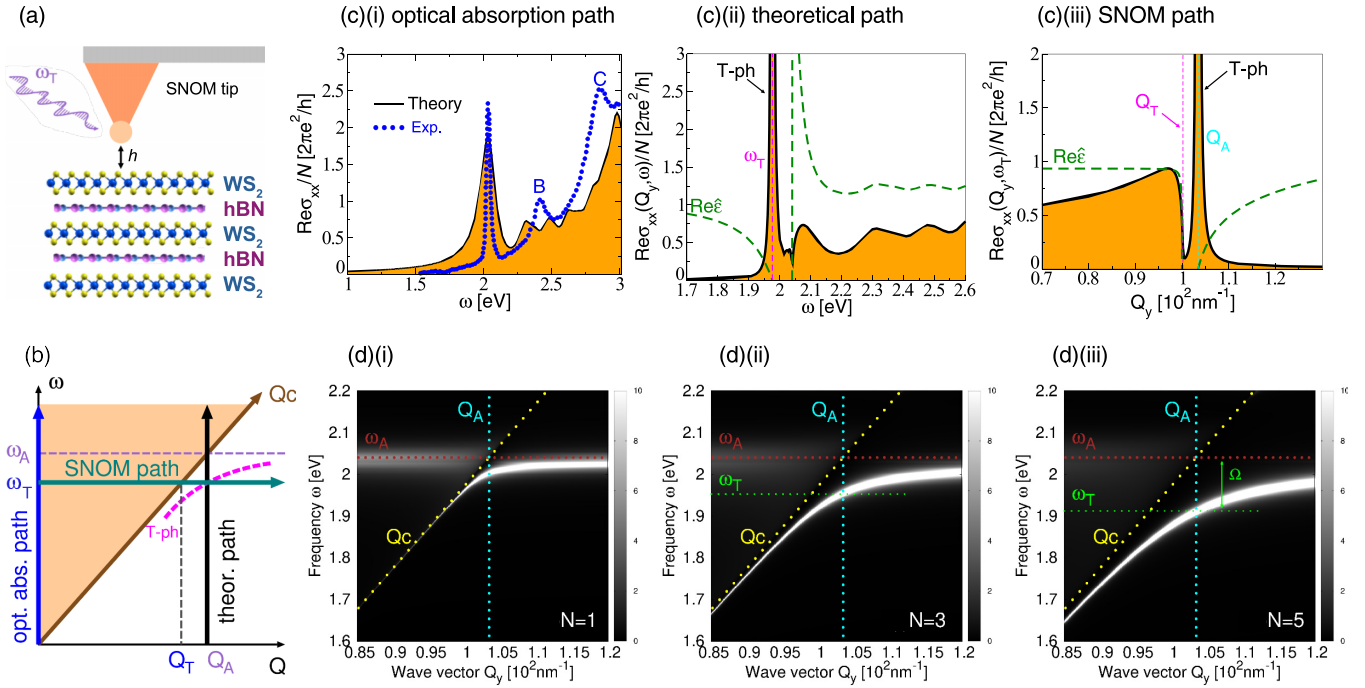
FIG. 1. (a) The s-SNOM setup consisting of a tip above the WS_2/hBN heterostructure. The incident photon at a fixed frequency ω_T is scattered in momentum space along the SNOM pathway. (b) Dispersion graph illustrating different scanning pathways in frequency and momentum space. The SNOM and theoretical pathways intersect with the T-ph mode (pink dashed line) while the optical absorption does not. The normalized conductivity ($\mathrm{Re}[\sigma_{xx}/N]$) in WS_2/hBN heterostructure along the (c)(i) experimental pathway [$\mathbf{Q} = (0, 0)$], (c)(ii) theoretical pathway $\mathbf{Q} = (0, Q_A)$, where $Q_A = \omega_A/c = 0.01 \, \mathrm{nm}^{-1}$, and (c)(iii) SNOM pathway $\mathbf{Q} = (0, Q_y)$. The A exciton energy is $\hbar\omega_A = 2.04 \, \mathrm{eV}$ and the experimentally measured conductivity [14] is denoted by blue dots in (c)(i). The driving frequency in (c)(ii) is $\omega_T = 1.96 \, \mathrm{eV}$. The number of WS_2 single layers is $N = 3$. The green dashed line in (c)(ii) and (c)(iii) shows $\mathrm{Re}[\det \hat{\epsilon}]$. The ($Q_y$, ω) scan of normalized conductivity $\mathrm{Re}[\sigma_{xx}/N]$ in (d)(i) WS_2 single layer ($N = 1$), (d)(ii) WS_2/hBN trilayer ($N = 3$), and (d)(iii) five layers ($N = 5$).

strength f_T [Eq. (7)] [2] and bending factor, i.e., the T-ph energy relative to the free-photon energy,

$$\Omega = Qc - \omega_T(\mathbf{Q}).$$

Here, both quantities (f_T and Ω) will be considered at wave vectors $Q_A = \omega_A/c = 0.0103 \, \mathrm{nm}^{-1}$ or $Q_g = E_g/c = 0.0129 \, \mathrm{nm}^{-1}$ at which the WS_2 A exciton $\hbar\omega_A = 2.04 \, \mathrm{eV}$ or band gap $E_g = 2.54 \, \mathrm{eV}$ crosses the light line Qc, and where we assume that T-ph has the highest spectral weight and bending. We will use the latter wave vector Q_g when we consider the results in the RPA model (where $\hat{\sigma}^{\mathrm{ladd}} = 0$). T-ph bending Ω is also depicted in Fig. 1(d)(iii). Figures 2(a) and 2(b) show f_T/N and Ω, respectively, in WS_2/hBN multilayers. In the RPA + ladder model (circles), the increase from $N = 1$ to $N = 5$ causes an oscillator strength enhancement of as much as 70%, and linear bending increases from $\Omega = 36 \, \mathrm{meV}$ to $\Omega = 128 \, \mathrm{meV}$. In the RPA model (squares) $N = 1$, the oscillator strength is much weaker but rapidly increases with layer number, so that for $N = 5$ one obtains a 15-fold enhancement. The RPA bending increases from 5 to 107 meV. If the heterostructure thickness is much smaller than the extent of the evanescent field ($l \ll 1/Q_A$), and because $\omega_T \ll E_g^{\mathrm{hBN}}$,[2] and $\lim_{\omega \to \omega_T} \sigma_\mu^{0,\mathrm{hBN}}(\omega) \approx 0$, its unscreened conductivity can

be approximated as

$$\sigma_x^0(\omega) \approx N\sigma_x^{0,\mathrm{WS}_2}(\omega), \tag{8}$$

and its transversal 2D dielectric function becomes [2]

$$\epsilon_x(Q_y, \omega) = 1 + N\frac{2\pi\omega}{\beta c^2}\sigma_x^{0,\mathrm{WS}_2}(\omega), \tag{9}$$

where $\beta = \sqrt{\gamma^2\omega^2 - Q_y^2}$, $\gamma = \frac{e^2}{\hbar c} = 1/137$ is the fine-structure constant, and $\sigma_x^{0,\mathrm{WS}_2}(\omega) = l_i\sigma_{xx,g=0,g'=0}^{0,i}(Q_y = 0, \omega)$ is the unscreened conductivity in WS_2 single layer. According to Eq. (7) the 2D T-ph normalized oscillatory strength then becomes [2]

$$f_x(Q_y)/N = \omega_T \mathrm{Im}\big[\sigma_x^{0,\mathrm{WS}_2}(\omega_T)\big]\bigg[\frac{\partial}{\partial\omega}\mathrm{Re}\,\epsilon_x(Q_y, \omega_T, N)\bigg]^{-1} \tag{10}$$

Simple 2D modeling (9) and (10) enables fast estimation of the energy and intensity of electromagnetic modes in multilayered systems, while shedding light on the mechanisms that give rise to them. For example, from Eq. (10) one concludes that T-ph exists only if $\mathrm{Im}[\sigma_x^{0,\mathrm{WS}_2}] < 0$, considering that $\mathrm{Re}[\partial\epsilon_x/\partial\omega] < 0$. Figures 2(a) and 2(b) show f_x/N and Ω, respectively, derived using 2D-RPA + ladder (diamonds) and 2D-RPA (stars) models. Remarkably, we can observe very good agreement between the 2D and full models.

For thicker composites $N \geqslant 10$, f_T/N saturates in both models, indicating that f_T scales with N as expected. However, for thicker layers, Ω continues to increase, in 2D-RPA +

---

[2]The hBN conductivity was calculated at the RPA level ($\sigma^0 = \sigma^{\mathrm{RPA}}$) and for its band gap we used the DFT value $E_g^{\mathrm{hBN}} = 4.5 \, \mathrm{eV}$.
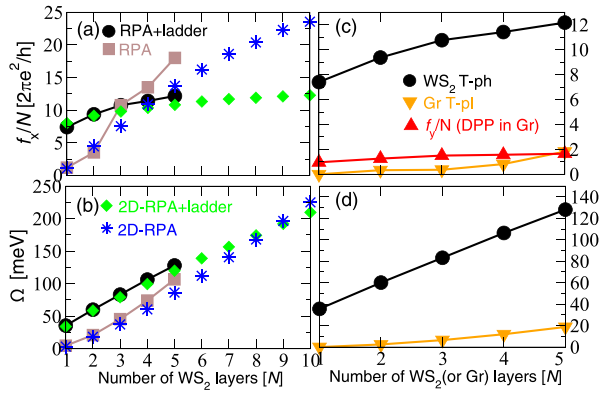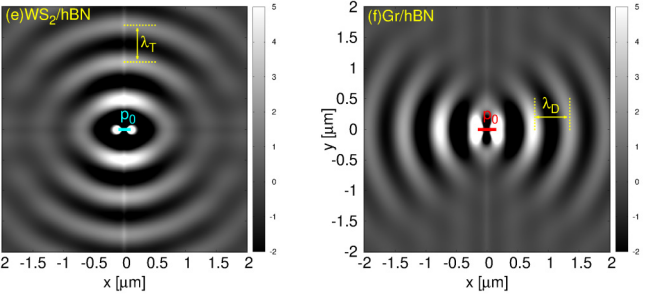
FIG. 2. (a) T-ph normalized oscillatory strength f_x/N and (b) bending Ω in WS$_2$/hBN multilayers obtained using (●) RPA + ladder, (■) RPA, (◆) 2D − RPA + ladder and (✳) 2D-RPA models. (c) The oscillatory strengths f_x/N of (●) T-ph in WS$_2$/hBN, (▼) the T-pl in Gr/hBN, and oscillatory strength f_y/N of (▲) DPP in Gr/hBN multilayers. (d) The bendings Ω of (●) T-ph in WS$_2$/hBN, and (▼) the T-pl in Gr/hBN multilayers. (e) The induced current $j_x^{ind}(\rho)$ in WS$_2$/hBN and in (f) Gr/hBN trilayers ($N = 3$) driven by point dipole $\mathbf{p} = (1, 0)$ oscillating at frequencies $\omega_T = 1.96$ eV and $\omega_D = 0.29$ eV, respectively. The Gr electron doping is $n = 1 \times 10^{14}$ cm^{-2} per layer.

ladder, almost linearly. This linear increase for larger N (referring to the bulk limit) still has to saturate because the maximum bending Ω is constrained by either ω_A or E_g. Achieving the saturation for large N using the full RPA + ladder model is computationally prohibitive, while the simple 2D-RPA + ladder model is no longer plausible for very thick ($l \sim 1/Q_A$) composites. To explore the limiting behavior we instead redefine the conductivity of the van der Waals composite with spatially separated 2D conductivities of WS$_2$ and hBN from Eq. (S26), allowing us to increase the number of layers up to $N = 60$ (see SM Sec. S2.G). While the saturation is still not fully achieved, another trend can be observed, namely that $\Omega(N \to \infty) \approx E_g/2$ in RPA or $\Omega(N \to \infty) \approx \omega_A/2$ in the RPA + ladder model. Consequently, as N goes to infinity, T-ph's phase velocity approaches half the speed of light $c/2$.

Finally, a clear existence of a strong and well-defined polariton mode in both models, i.e., with and without excitonic effects, confirms the plasmonic rather than excitonic nature of T-ph, even though the relevant electronic transitions are interband transitions across the gap.

Figure 2(c) depicts oscillatory strengths f_x/N of T-ph in WS$_2$/hBN (dots) and of T-pl in Gr/hBN (triangle down) heterostructures. For graphene, we assume that the strongest oscillator strength occurs when light-line Qc crosses the interband excitations gap, i.e., for $Q_F = 2E_F/c$. The electron concentration is chosen to be $n = 1 \times 10^{14}$ cm^{-2} corresponding to $E_F = 1$ eV and $Q_F = 0.0101$ nm^{-1}. It can be seen that T-ph in WS$_2$ is about two orders of magnitude stronger than T-pl in Gr. For example, T-ph in WS$_2$ bilayer is 29 times stronger than T-pl in Gr bilayer ($N = 2$). The triangles in Fig. 2(c) show the oscillator strength f_y/N of Gr longitudinal DPP calculated for the wave vector $Q_A = 0.0103$ nm^{-1}. Remarkably, the T-ph mode exhibits significantly greater strength than the DPP mode for all thicknesses, with an increase of more than sevenfold observed in the bilayer ($N = 2$). Figure 2(d) depicts the bending Ω of T-ph in WS$_2$/hBN (dots) and of T-pl in Gr/hBN (triangle down) heterostructures. As anticipated, the T-ph bending mode is considerably stronger than the T-pl bending mode in WS$_2$ heterostructures, with a difference of about 25 times for the bilayers ($N = 2$). Overall, our assess-

ments suggest that the T-ph mode in WS$_2$ heterostructures has the potential to be a significantly stronger mode compared to the commonly known T-pl and DPP modes observed in doped graphene.

Below we simulate s-SNOM measurements, also used to determine DPP in doped graphene [35,36]. We suppose that the SNOM tip is at a height $h = 50.0$ nm relative to the topmost atomic layer occupying the $z = 0$ plane [see Fig. 1(a)]. The tip was approximated as an oscillating dipole $\mathbf{p}_0 \sin(\omega_T t)$ localized at a point $\mathbf{r}_0 = (\boldsymbol{\rho}_0, h)$ so that the (z-integrated) induced current is [2]

$$\mathbf{j}_{\text{ind}}(\boldsymbol{\rho}, t) = \omega_T \text{Re} \int \frac{d\mathbf{Q}}{(2\pi)^2} e^{i\beta h} e^{i\mathbf{Q}\boldsymbol{\rho}} e^{-i\omega_T t}$$
$$\times \hat{\sigma}(\mathbf{Q}, \omega_T) \hat{\Gamma}(\mathbf{Q}, \omega_T) \mathbf{p}_0. \quad (11)$$

Figure 2(e) shows the induced current $j_x(\boldsymbol{\rho})$ in WS$_2$/hBN trilayer ($N = 3$) driven by a point dipole $\mathbf{p} = (1, 0)$ and $\omega_T = 1.96$ eV. The induced wave of wavelength $\lambda_T \approx 600$ nm (which agrees well with $2\pi/Q_A = 607$ nm) propagating along the y direction (perpendicular to current) is the T-ph mode. Figure 2(f) shows the same in the Gr/hBN trilayer where the driving frequency is $\omega_D = 0.29$ eV corresponding to the DPP energy in the Gr/hBN trilayer at $Q = Q_A$ where the electron doping per graphene layer is $n = 1 \times 10^{14}$ cm^{-2}. The induced wave of wavelengths $\lambda_D \approx 580$ nm propagating in the x direction (parallel to the current) represents the longitudinal DPP. Comparing the intensities and Fourier purity of the induced patterns, we conclude that the T-ph mode in the WS$_2$ heterostructure should be observable in a s-SNOM setup in the same manner as DPP is routinely observed in doped graphene [35,36].

Below we prove that T-ph exists in any 2D configuration that supports dipole-active electronic transitions. In the Supplemental Material [2] we consider a 2D rectangular lattice of identical atoms (or molecules) where each site supports one dipole-active transition between highest occupied molecular orbital (HOMO) and lowest unoccupied molecular orbital (LUMO) states $(E_p, \phi_p) \to (E_d, \phi_d)$. The HOMO-LUMO band gap is $\Delta = E_d - E_p$ and the 2D unit cell surface is S_{uc}.

We derive that this 2D configuration supports two (listed here only for $Q_y = \gamma \Delta$) electromagnetic modes, the longitudinal (L) Frenkel exciton $\omega_L = \Delta$ and the transverse (T) mode (which *does not* exist in the nonretarded limit $\gamma \to 0$)

$$\omega_T = \omega_L - \frac{1}{2} \left(\frac{\alpha^2 \gamma^2}{\Delta} \right)^{1/3}, \tag{12}$$

where $\alpha = \frac{4\pi |j_x|^2}{S_{uc}}$. The on-site dipole matrix elements is $j_\mu = \frac{1}{2i} \int_{\Omega_{uc}} d\mathbf{r} \{ \phi_d^* \partial_\mu \phi_p - [\partial_\mu \phi_d^*] \phi_p \}$. The L-T splitting (12) is here also identified as T-mode bending $\Omega = \omega_L - \omega_T$ which is obviously (due to fine structure γ) very weak. However, Ω could be increased by increasing the dipole matrix element j_x and/or the density of dipoles $1/S_{uc}$. The latter can be increased by, for example, increasing the number of dipolar layers N, which according to Eq. (8) provides simple scaling low $\Omega \sim N^{2/3}$. The effect also appears to be stronger in systems with smaller band gaps Δ.

In conclusion, our theoretical study reveals that trapped photons are a ubiquitous feature of all layered semiconduct- ing crystals, and are in all their properties counterparts of 2D plasmon modes in conductive crystals. In other words, semiconducting heterostructures are characterized by transverse plasmon polaritons built from interband electron-hole transitions and a photon. Unlike the longitudinal 2D plasmon mode, whose intensity and energy can be modified by doping, the trapped-photon mode can be modified by stacking the different numbers and types of layers in the van der Waals composite. We anticipate that semiconducting heterostructures and their transverse plasmon mode could have an equally or even more significant role in applied plasmonics and photonics compared to well-established metallic layers supporting longitudinal plasmons.

[1] A. N. Grigorenko, M. Polini, and K. Novoselov, Nat. Photonics **6**, 749 (2012).

[2] See Supplemental Material at http://link.aps.org/supplemental/10.1103/PhysRevB.108.L121402 for more details on the system geometry, theoretical approach, limiting cases, and computational details, which includes Refs. [43–58].

[3] E. A. Vinogradov, Phys. Rep. **217**, 159 (1992).

[4] J. Pitarke, V. Silkin, E. Chulkov, and P. Echenique, Rep. Prog. Phys. **70**, 1 (2006).

[5] D. N. Basov, A. Asenjo-Garcia, P. J. Schuck, X. Zhu, and A. Rubio, Nanophotonics **10**, 549 (2021).

[6] D. Novko, K. Lyon, D. J. Mowbray, and V. Despoja, Phys. Rev. B **104**, 115421 (2021).

[7] V. Despoja and L. Marušić, Int. J. Mol. Sci. **23**, 6943 (2022).

[8] D. Pines and P. Nozieres, *Theory of Quantum Liquids*, Vol. I (CRC Press, Boca Raton, FL, 1999).

[9] S. A. Mikhailov and K. Ziegler, Phys. Rev. Lett. **99**, 016803 (2007).

[10] D. Novko, M. Šunjić, and V. Despoja, Phys. Rev. B **93**, 125413 (2016).

[11] M. Jablan, H. Buljan, and M. Soljačić, Opt. Express **19**, 11236 (2011).

[12] T. Low, A. Chaves, J. D. Caldwell, A. Kumar, N. X. Fang, P. Avouris, T. F. Heinz, F. Guinea, L. Martin-Moreno, and F. Koppens, Nat. Mater. **16**, 182 (2017).

[13] A. Ramasubramaniam, Phys. Rev. B **86**, 115409 (2012).

[14] Y. Li, A. Chernikov, X. Zhang, A. Rigosi, H. M. Hill, A. M. van der Zande, D. A. Chenet, E.-M. Shih, J. Hone, and T. F. Heinz, Phys. Rev. B **90**, 205422 (2014).

[15] D. Y. Qiu, F. H. da Jornada, and S. G. Louie, Phys. Rev. Lett. **111**, 216805 (2013).

[16] Y. Lin, X. Ling, L. Yu, S. Huang, A. L. Hsu, Y.-H. Lee, J. Kong, M. S. Dresselhaus, and T. Palacios, Nano Lett. **14**, 5569 (2014).

[17] J. Yan, K. W. Jacobsen, and K. S. Thygesen, Phys. Rev. B **86**, 045208 (2012).

[18] F. Ferreira and R. M. Ribeiro, Phys. Rev. B **96**, 115431 (2017).

[19] C. E. Villegas, A. Rodin, A. Carvalho, and A. Rocha, Phys. Chem. Chem. Phys. **18**, 27829 (2016).

[20] X. Wang, A. M. Jones, K. L. Seyler, V. Tran, Y. Jia, H. Zhao, H. Wang, L. Yang, X. Xu, and F. Xia, Nat. Nanotechnol. **10**, 517 (2015).

[21] X. Liu, T. Galfsky, Z. Sun, F. Xia, E.-c. Lin, Y.-H. Lee, S. Kéna-Cohen, and V. M. Menon, Nat. Photonics **9**, 30 (2015).

[22] S. Dufferwiel, S. Schwarz, F. Withers, A. Trichet, F. Li, M. Sich, O. Del Pozo-Zamudio, C. Clark, A. Nalitov, D. Solnyshkov *et al.*, Nat. Commun. **6**, 8579 (2015).

[23] L. C. Flatten, Z. He, D. M. Coles, A. A. Trichet, A. W. Powell, R. A. Taylor, J. H. Warner, and J. M. Smith, Sci. Rep. **6**, 33134 (2016).

[24] S. Dufferwiel, T. Lyons, D. Solnyshkov, A. Trichet, A. Catanzaro, F. Withers, G. Malpuech, J. Smith, K. Novoselov, M. Skolnick *et al.*, Nat. Commun. **9**, 4797 (2018).

[25] J. Gu, V. Walther, L. Waldecker, D. Rhodes, A. Raja, J. C. Hone, T. F. Heinz, S. Kéna-Cohen, T. Pohl, and V. M. Menon, Nat. Commun. **12**, 2269 (2021).

[26] M. Förg, L. Colombier, R. K. Patel, J. Lindlau, A. D. Mohite, H. Yamaguchi, M. M. Glazov, D. Hunger, and A. Högele, Nat. Commun. **10**, 3697 (2019).

[27] Z. Fei, M. E. Scott, D. J. Gosztola, J. J. Foley, IV, J. Yan, D. G. Mandrus, H. Wen, P. Zhou, D. W. Zhang, Y. Sun, J. R. Guest, S. K. Gray, W. Bao, G. P. Wiederrecht, and X. Xu, Phys. Rev. B **94**, 081402(R) (2016).

[28] D. Novko and V. Despoja, Phys. Rev. Res. **3**, L032056 (2021).

[29] V. Despoja and D. Novko, Phys. Rev. B **106**, 205401 (2022).

[30] R. Verre, D. G. Baranov, B. Munkhbat, J. Cuadra, M. Käll, and T. Shegai, Nat. Nanotechnol. **14**, 679 (2019).

[31] S. S. Sinha, A. Zak, R. Rosentsveig, I. Pinkas, R. Tenne, and L. Yadgarov, Small **16**, 1904390 (2020).

[32] H. Zhang, B. Abhiraman, Q. Zhang, J. Miao, K. Jo, S. Roccasecca, M. W. Knight, A. R. Davoyan, and D. Jariwala, Nat. Commun. **11**, 3552 (2020).

[33] S. B. Anantharaman, K. Jo, and D. Jariwala, ACS Nano **15**, 12628 (2021).

[34] B. Munkhbat, D. G. Baranov, M. Stührenberg, M. Wersäll, A. Bisht, and T. Shegai, ACS Photonics **6**, 139 (2018).

[35] Z. Fei, G. O. Andreev, W. Bao, L. M. Zhang, A. S. McLeod, C. Wang, M. K. Stewart, Z. Zhao, G. Dominguez, M. Thiemens *et al.*, Nano Lett. **11**, 4701 (2011).

[36] Z. Fei, A. Rodin, G. O. Andreev, W. Bao, A. McLeod, M. Wagner, L. Zhang, Z. Zhao, M. Thiemens, G. Dominguez *et al.*, Nature (London) **487**, 82 (2012).

[37] C. Hu, A. Deng, P. Shen, X. Luo, X. Zhou, T. Wu, X. Huang, Y. Dong, K. Watanabe, T. Taniguchi *et al.*, Nanoscale **13**, 14628 (2021).

[38] A. Singh, H. Y. Lee, and S. Gradečak, Nano Res. **13**, 1363 (2020).

[39] P. Nagler, M. V. Ballottin, A. A. Mitioglu, M. V. Durnev, T. Taniguchi, K. Watanabe, A. Chernikov, C. Schüller, M. M. Glazov, P. C. M. Christianen, and T. Korn, Phys. Rev. Lett. **121**, 057402 (2018).

[40] A. Di Renzo, O. Çakıroğlu, F. Carrascoso, H. Li, G. Gigli, K. Watanabe, T. Taniguchi, C. Munuera, A. Rizzo, A. Castellanos-Gomez *et al.*, Nanomaterials **12**, 4425 (2022).

[41] G. Haider, K. Sampathkumar, T. Verhagen, L. Nádvorník, F. J. Sonia, V. Valeš, J. Sýkora, P. Kapusta, P. Němec, M. Hof *et al.*, Adv. Funct. Mater. **31**, 2102196 (2021).

[42] X. Zhao, Z. Cui, A. Ge, X. Lu, X. Guan, J. Zhang, H. Zhen, L. Sun, S. Wang, and W. Lu, Appl. Phys. Lett. **121**, 231106 (2022).

[43] M. Tomaš, Phys. Rev. A **51**, 2545 (1995).

[44] V. Despoja, M. Šunjić, and L. Marušić, Phys. Rev. B **80**, 075410 (2009).

[45] M. S. Hybertsen and S. G. Louie, Phys. Rev. B **34**, 5390 (1986).

[46] M. Rohlfing and S. G. Louie, Phys. Rev. Lett. **83**, 856 (1999).

[47] M. Rohlfing and S. G. Louie, Phys. Rev. B **62**, 4927 (2000).

[48] P. Giannozzi, S. Baroni, N. Bonini, M. Calandra, R. Car, C. Cavazzoni, D. Ceresoli, G. L. Chiarotti, M. Cococcioni, I. Dabo *et al.*, J. Phys.: Condens. Matter **21**, 395502 (2009).

[49] J. P. Perdew, K. Burke, and M. Ernzerhof, Phys. Rev. Lett. **77**, 3865 (1996).

[50] H. J. Monkhorst and J. D. Pack, Phys. Rev. B **13**, 5188 (1976).

[51] A. Chernikov, T. C. Berkelbach, H. M. Hill, A. Rigosi, Y. Li, B. Aslan, D. R. Reichman, M. S. Hybertsen, and T. F. Heinz, Phys. Rev. Lett. **113**, 076802 (2014).

[52] A. Chernikov, A. M. van der Zande, H. M. Hill, A. F. Rigosi, A. Velauthapillai, J. Hone, and T. F. Heinz, Phys. Rev. Lett. **115**, 126802 (2015).

[53] H. T. Nguyen, T. J. Kim, H. G. Park, X. A. Nguyen, D. Koo, C.-H. Lee, S. C. Hong, Y. D. Kim *et al.*, Appl. Surf. Sci. **511**, 145503 (2020).

[54] B. Zhu, X. Chen, and X. Cui, Sci. Rep. **5**, 9218 (2015).

[55] J. Jung, A. Raoux, Z. Qiao, and A. H. MacDonald, Phys. Rev. B **89**, 205414 (2014).

[56] K. Berland and P. Hyldgaard, Phys. Rev. B **89**, 035412 (2014).

[57] A. Dal Corso, Comput. Mater. Sci. **95**, 337 (2014).

[58] M. J. van Setten, M. Giantomassi, E. Bousquet, M. J. Verstraete, D. R. Hamann, X. Gonze, and G.-M. Rignanese, Comput. Phys. Commun. **226**, 39 (2018).